Synchrotron Refraction CT and Synchrotron Bragg Magnification CT for NDE

B.R. Müller, A. Lange, M. Harwardt, M.P. Hentschel, B. Illerhaus, J. Goebbels

Radiological Methods, Federal Institute for Materials Research and Testing (BAM); Berlin, Germany;
Phone: +49 (0) 30 8104 4635, Fax +49 (0) 30 8104 1837; e-mail: bernd.mueller@bam.de

Abstract
X-Ray Refraction Topography techniques are based on Ultra Small Angle Scattering by micro structural elements causing phase related effects like refraction and total reflection at a few minutes of arc as the refractive index of X-rays is nearly unity. The refraction contrast is several times higher than "true absorption" and results in images of cracks, pores and fibre debonding separations below the spatial resolution of the detector. In most cases the investigated inner surface and interface structures correlate to mechanical properties. For the exploration of micro structured materials the refraction technique has been improved by a 3D Synchrotron Refraction Computed Tomography test station. The specimen is placed in an X-ray beam between two single crystals, which suppresses all sample scattering. In addition an asymmetric cut second crystal can magnify the image up to 50 times revealing nano meter resolution. The technique is an alternative to other attempts on raising the spatial resolution of CT machines.
Keywords: X-ray Refraction, Diffraction Enhanced Imaging (DEI), Bragg Magnification, Synchrotron Radiation, Computed Tomography (CT), Metal Matrix Composites (MMC), Lightweight Materials, Aerospace

1. Introduction

In computed tomography the contrast at interfaces within heterogeneous materials can be strongly amplified by effects related to X-ray refraction. Such effects are especially useful for materials of low absorption or mixed phases showing similar X-ray absorption properties which produce low contrast. X-Ray refraction is an Ultra Small-Angle Scattering (USAXS) phenomenon [1, 2]. Refraction contrast is also applied for planar refraction topography, a scanning technique for improved non-destructive characterization of high performance composites, ceramics and other low density materials and components [3]. X-ray refraction occurs whenever X-rays interact with interfaces (cracks, pores, particles, phase boundaries) especially at low angles of incidence. This is in analogy to the behaviour of visible light in transparent materials e.g. lenses or prisms. X-ray optical effects can be observed at small scattering angles of between several seconds and a few minutes of arc as the refractive index *n* of X-rays is nearly unity. In other terms, due to the short X-ray wavelength below 0.1nm X-ray 'light scattering' is sensitive to inner surfaces and interfaces of nanometre dimensions.

2. Physical Background

In analogy to visible optics the interaction of X-rays with small transparent structures above several nanometres size results in coherent scattering governed by wavelength, structural dimensions and shape, local phase shift and absorption. In contrast to optical conditions the refractive index of X-rays close to unity causes beam deflections into the same small angular region of several minutes of arc as does diffraction. Thus the resulting interferences are due to phase modulation due to the refractive index and the absorptive and Raleigh diffraction, both depending on the path length through matter. However, if the dimensions of the scattering objects are much larger than several tens of

nanometres as it is common in classical small-angle scattering, the interference fringes are not observable any more by classical small-angle cameras as they are too narrow. The resulting smeared angular intensity distribution is then simply described by a continuous decay according to the laws of refraction by transparent media, e.g. applying Snell's law [2]. This purely geometrical refraction approach is appropriate for small-angle X-ray (and neutron) scattering effects by micrometer sized structures and applied in the following.

2.1 Refraction Effect

If ε is the real term of the (generally) complex index of refraction n', ρ_e the electron density and λ the X-ray wavelength then the real part n is:

$$n = 1 - \varepsilon \text{, with } \varepsilon \approx \rho_e \cdot \lambda^2 \quad \text{.....(1)}$$

For glass and 8 keV X-ray photon energy $\varepsilon \cong 1 \cdot 10^{-5}$. In contrast to light optics convex lenses cause divergence of X-rays as $n < 1$. Figure 1 left demonstrates the effect of small-angle scattering by refraction of cylindrical lenses. A bundle of glass fibres (15 µm fibre diameter) deflects a pinhole-collimated X-ray beam by several minutes of arc. In fibres and spherical particles deflection of X-rays occurs twice, namely when entering and when leaving the object (see inset in Fig. 1 left). The resulting intensity distribution is measured by an X-ray film or a CCD-camera while the straight (primary) beam is eliminated by a beam stop. The shape of the intensity distribution of such cylindrical objects is a universal function independent of materials if the scattering angle is normalized to the critical angle Θ_c of total reflection (see Fig. 1 right) defined by the refractive index $\Theta^2_c = 2\varepsilon$. The intensity of the deflected X-rays is nearly zero at the critical angle (see Fig. 1 right), with a small contribution from total reflection.

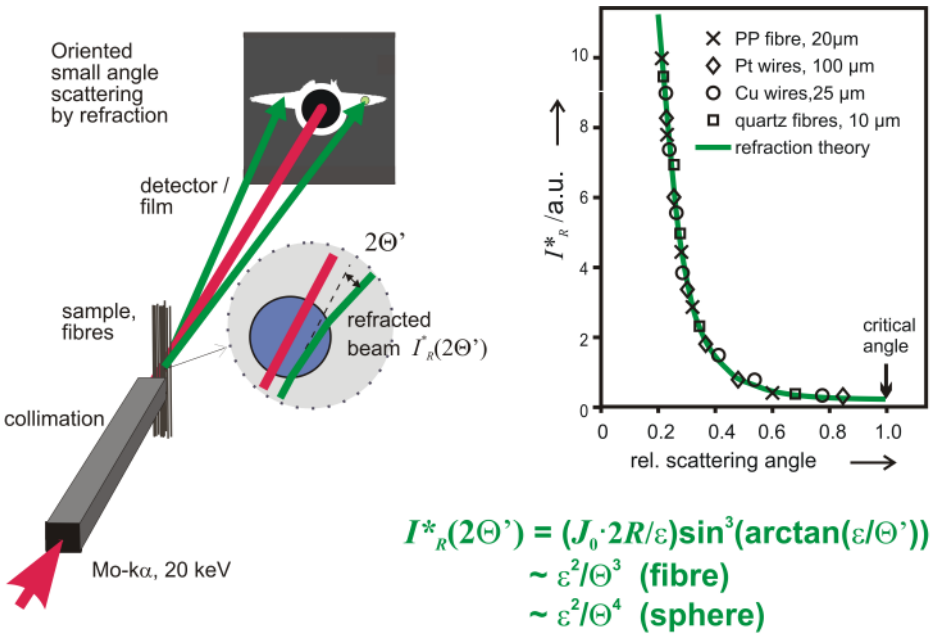

Figure 1. Left: Effect of oriented small-angle scattering by refraction on glass fibres. Right: Normalized profile of the angular intensity distribution of cylindrical objects (PP = polypropylene).

A cross section of 1×10^{-3} of the fibre diameter contributes to the detectable intensity above a scattering angle of typically 2 minutes of arc. Total reflection of X-rays occurs as well, but only a small fraction ($\approx1\cdot10^{-6}$) of the cylinder diameter is involved and therefore negligible. However, planar surfaces may scatter all the primary intensity if they are well aligned. Based on Snell's law the angular intensity distribution of cylinders has been modelled and fitted to measurements on a number of different fibres, as illustrated by Figure 1 right. The refracted intensity I^*_R of a cylinder (without absorption effects) can be expressed by [2]:

$$I_R^*(2\Theta') = \frac{J_0 \cdot 2R}{\varepsilon} \cdot \sin^3\left(\arctan\frac{\varepsilon}{\Theta'}\right) \cong \frac{J_0 \cdot 2R \cdot \varepsilon^2}{\Theta^3} \quad \text{.....(2)}$$

J_0 is the irradiation density of the incident X-rays, R is the cylinder radius and $2\Theta' = \Theta$ is the scattering angle. For spherical particles or pores I^*_R becomes:

$$I_R^*(2\Theta') \cong \frac{J_0 \cdot 2R \cdot \varepsilon^2}{\Theta^4} \quad \text{.....(3)}$$

The conventional understanding of 'continuous' small-angle X-ray scattering (SAXS) is governed by the interpretation of diffraction effects. Both the well known Guinier theory [4] for separated particles and Porod theory [5] of densely packed colloids are based on diffraction related to Raleigh scattering. Porod approximates the same angular intensity decay as in eqn. 3. However, both diffraction approaches are related to scattering objects two orders of magnitude smaller.

2.2 Refraction Tomography

Refraction tomography by conventional X-ray tubes has some disadvantages. It is restricted to low X-ray energies given by the characteristic emission of Cu- or Mo-targets in X-ray tubes and thus to low density materials. The thickness of the investigated samples is limited to a few millimetres and much smaller in case of metals. The measurements require several hours because the specimen has to bee scanned and rotated across a very narrow beam.

2.2.1 Experimental Set-Up

In order to overcome the above mentioned limitations 3D synchrotron refraction tomography (SyRef-CT) is employed. At the hard X-ray experimental station (BAM*line*) [6] at the Berliner Electron Storage Ring for Synchrotron Radiation (BESSY) in Berlin, Germany the available monochromatic photon energy ranges from 5 keV up to 80 keV. The experimental set-up is defined by Figure 2 top [7] and has become known as Diffraction Enhanced Imaging (DEI) in medical publications [8]. A parallel and monochromatic beam from the double multiplayer monochromator (DMM) or the double crystal monochromator (DCM) of the BAM*line* with a band width of about 2% or 0.2% is used, respectively. While the horizontal width of the beam is limited by the detector width the vertical size may be smaller than the camera height and varies with the used photon energy (the higher the energy the narrower the beam height due to the limited mirror or crystal length, respectively). The 50 keV photon

beam from the DMM has a horizontal width of up to 30 mm and a vertical width of a few millimetres, respectively. The beam is reflected by two Si(111) single crystals in a symmetric configuration. They are set to their Bragg angles for the chosen energy. The X-ray sensitive camera system is placed behind the second crystal and detects the photons reflected by the second crystal. The lateral resolution depends on the used microscope optics of the camera system and varies from 10.7×10.7 µm2 to 1.5×1.5 µm^2, respectively.

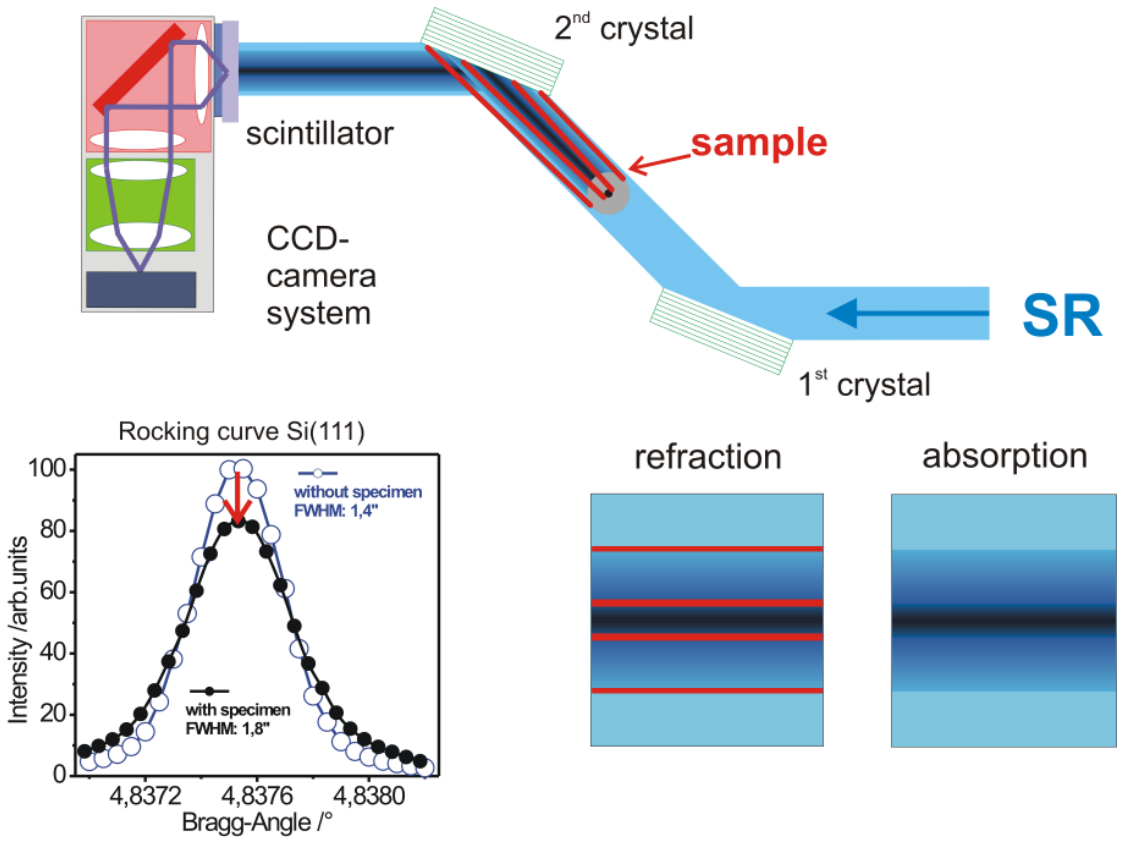

Figure 2. Top: Sketch of the experimental set up. The refracted rays are blocked by the 2nd crystal (red rays). Bottom left: Rocking curve of the Si(111) single crystal pair in symmetric configuration at 50 keV with specimen (filled dots) and without specimen (open circles) between the two crystals. The area under the curves is set to equal. Bottom right: demonstration of the refraction enhanced contrast.

The rocking curve of the crystal pair is recorded by tilting the 2nd crystal against the 1st crystal around the Bragg angle while measuring the reflected intensity. The width of the rocking curve for Si(111) at 50 keV was FWHM = 1.404 arc-seconds (Fig. 2 bottom left, open circles). Differing from the set up for phase contrast CT measurements, the sample is positioned in the X-ray beam between the two crystals. The highly collimated and monochromatized beam from the 1st crystal transmits the specimen and will be attenuated according to the absorption properties of the sample. Additionally, x-rays are deflected at all interfaces in the sample due to the refraction effect. This leads to a broadening of the rocking curve to a FWHM = 1.764 arc-second (Fig. 2 bottom left, filled circles). As a consequence all scattered x-rays get lost at the 2nd crystal, if the crystal pair is set to the rocking curve maximum. This is illustrated in Figure 2 bottom right. The refracted x-rays from the inner surfaces of the specimen are blocked by the 2nd crystal (red rays in Fig. 2). This leads to a significant contrast enhancement in the

radiography of the sample (marked by red stripes on the refraction picture at bottom right of Fig. 2). If the 2nd crystal is slightly off the rocking curve maximum only the scattered X-rays will be reflected and detected by the CCD-camera system.

2.2.2. Measurements and Results

In an aircraft project cylindrical specimens with a diameter of about 3.5 mm have been provided by MTU Aero Engines. As reinforcing fibre the SCS6-fibre from Textron was taken. It has a 33 µm diameter carbon fibre as a core with a 1 µm pyro-C-protective coating, followed by SiC and again by a pyro-C-protective coating of 3 µm. The overall diameter of the fibre measures 140 µm. The fibres are coated (30 µm) with the titanium base alloy Ti6242 by magnetron sputtering and then bundled and formed by Hot Isostatic Pressing (HIP). Static and cyclic forces were applied in parallel to the fibres in order to obtain the values of several mechanical parameters. After the tests the specimens were examined by metallographic methods and the fractured surfaces were analysed.

After the mechanical treatments a conventional 3D absorption tomography investigation was carried out employing a fine-focus X-ray tube operated at 100 kV tube voltage. Figure 3 left shows the density reconstruction of one out of 300 planes with 4.7×4.7×4.7 µm^3 Voxel resolution (720 projections, rotation around cylinder axes, Fourier filtered back projection). It shows an axial section of a low-cycle fatigue (LCF) sample. Higher density appears green, low density appears blue, respectively. The reinforcing SiC-fibres appear as blue discs. In the selected plane of Figure 3 left a blue shaded area at the right indicates the presence of cracks which reduce absorption.

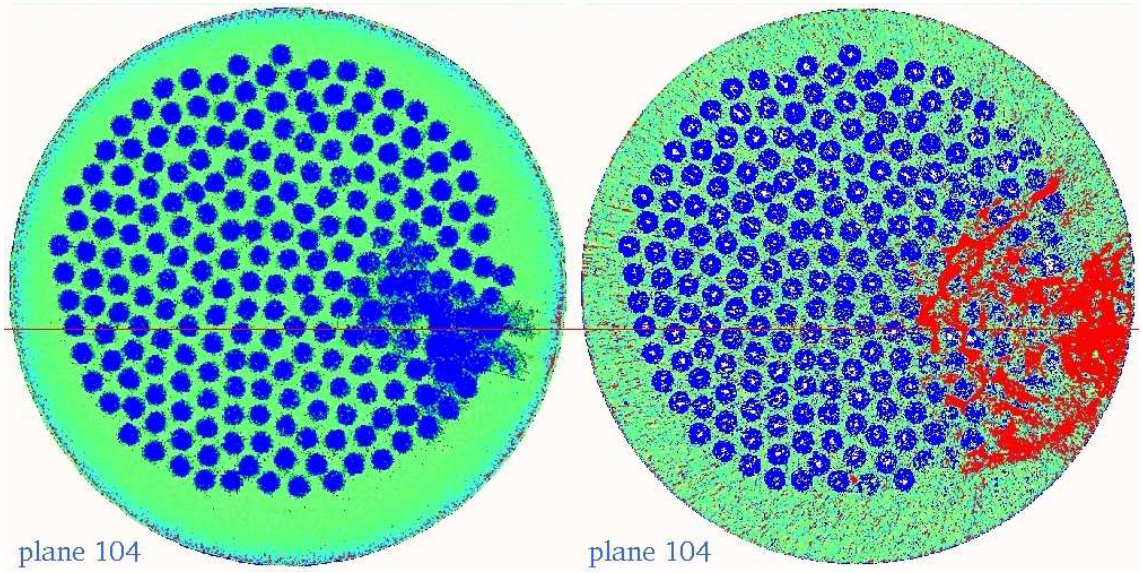

Figure 3. Left: Reconstruction (single slice) of conventional 3D absorption measurement on a Ti-SiC MMC specimen (3.5 mm diameter) after fatigue testing. Fine-focus tube 100 kV, 4.7×4.7×4.7 µm^3 Voxel. Right: Reconstruction (same specimen, same slice as left) of the 3D synchrotron refraction measurement. 50 keV monochromatic radiation, 5.3×5.3×5.3 µm^3 Voxel. Specimen is between the two crystals.

As a new approach for non-destructive testing the specimens were investigated by 3D Synchrotron Refraction Computed Tomography (SyRef-CT) at the BAMline at 50 keV photon energy and 5.3×5.3×5.3 µm^3 detector Voxel resolution (360 projections, Fourier filtered parallel beam back projection). The reconstruction of Figure 3 right shows the

same cross section of the LCF specimen as the left side, but now the crack area appears red (contrast enhanced) and is much more detailed and larger compared to the absorption results. Furthermore the low dense carbon core of the fibres can be seen as white dots in the centre of the blue disks. In contrast to conventional absorptive tomography refraction contrast provides evidence for the occurrence of cracks in about 20% of the 300 reconstructed slices of the specimen [7].
The high inverse contrast in Figure 3 right compared to the left side stems from the rejection of deflected X-rays by the 2nd crystal in front of the CCD-camera system due to refraction and total reflection at the crack boundaries. Refraction contrast is nearly independent of the crack width as it is a surface effect, but the contrast depends strongly on the incident angle of the beam onto the crack surface (e.g. for plane cracks the incident angel has to be in between ±1° as the index of refraction is nearly one – see Fig. 1 right). In the given measurement both crystals have been set to the top of their rocking curves. In this configuration Figure 3 right contains the information from absorption and refraction. If desired the 2nd crystal can be set outside the rocking curve centre. In this configuration only information from refraction will be shown in the image.

3. Magnification by asymmetric Bragg reflection

The lower limit of the lateral resolution of the camera system is determined by the microscope optics, including the luminescence screen and the CCD chip and is considered to be about 1 µm [9]. One approach to achieve sub micrometer resolution is the use of asymmetric Bragg reflections as a beam width magnifier in front of the detector system.

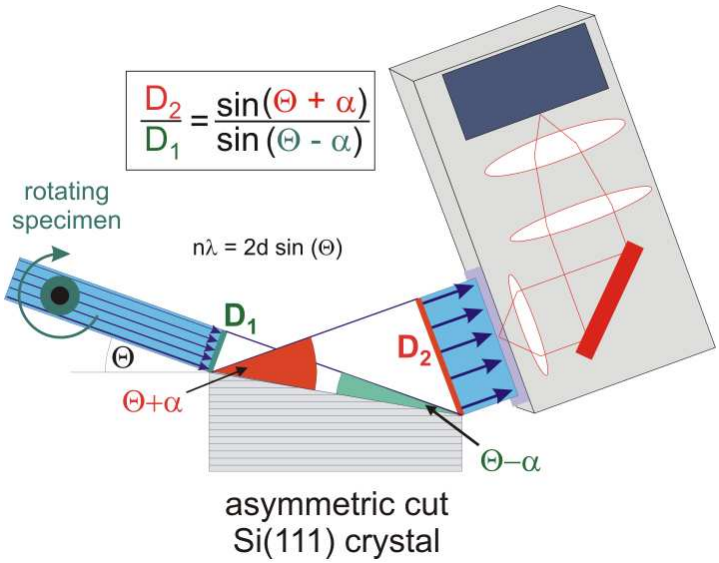

Figure 4. Principle of an one-dimensional beam width magnification by use of an asymmetric cut Bragg crystal. D1 and D2, width of the incoming and reflected beam, respectively. λ: Wavelength of the X-rays, d: distance between net planes of the crystal, Θ: gracing angle between beam and net plans, α: angle between surface and reflecting net planes of the crystal.

The well known method is based on the use of asymmetric cut Bragg crystals where the crystal surface is inclined by an asymmetry angle α against the reflecting lattice planes (see Fig. 4). The incoming parallel and monochromatic beam impinges on the inclined

crystal surface and will be reflected by the crystal lattice planes if the Bragg equation is fulfilled. According to the geometry shown in Figure 4 the reflected beam is magnified in one dimension. The magnification is defined by the equation given in Figure 4. For a given asymmetry angle α of the crystal the magnification can by varied (up to a factor of 50 or even more) by changing the photon energy of the incoming beam. In 1980 a resolution of about 0.5 µm was already reported by Förster [10]. A magnification in two dimensions by use of two asymmetric Bragg reflections was realized by Köhler [11]. For several questions concerning materials characterization by X-ray radiography a sub micrometer resolution in one-dimension is sufficient. A two-dimensional sub micrometer resolution can be archived by combining the Bragg magnification with the CT technique. This was done at the BAM*line* by using the experimental set up for the refraction CT shown in Figure 2. The analyser crystal (2^{nd} crystal) was replaced by an asymmetric cut Bragg crystal with an appropriate asymmetry angle. The axis of rotation of the specimen can be aligned perpendicular or parallel to the scattering plane of the crystal. This defines the orientation of the magnification plane in the reconstruction.

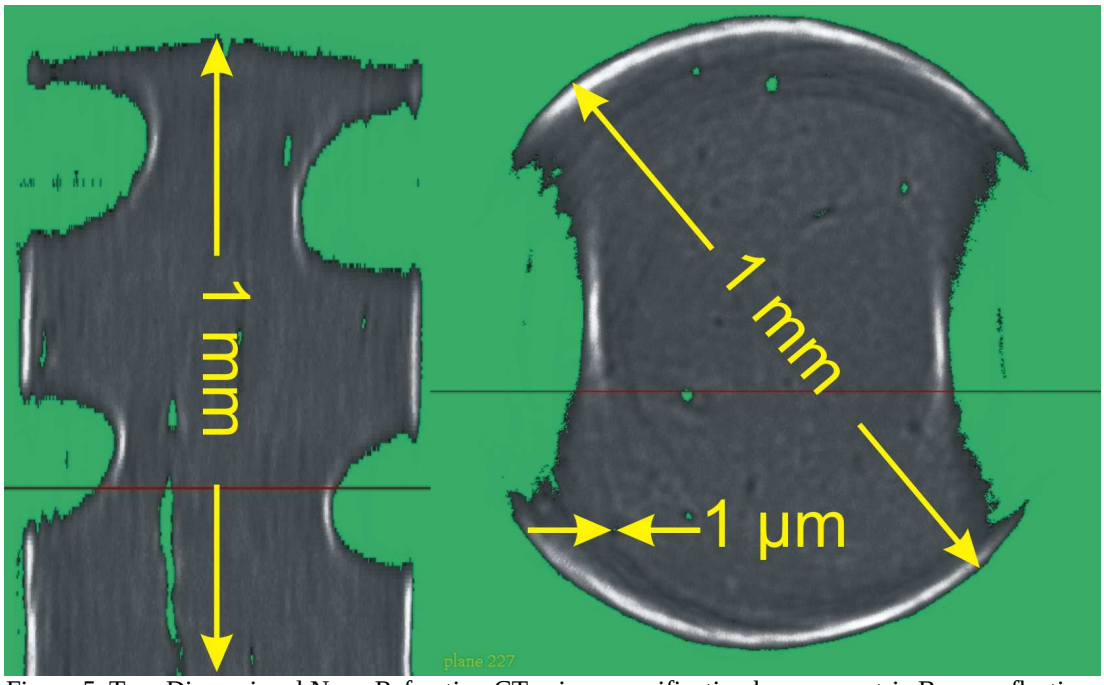

Figure 5. Two-Dimensional Nano Refraction CT using magnification by asymmetric Bragg reflection; reconstructed sagittal (left) and axial (right) plane of a steel micro drill from 19 keV projections; green tubular pores below 1 µm diameter and refraction contrast at outer edges and around pores is visible.

As an example a stainless steel micro drill (100 µm diameter, 1 mm length) was investigated at 19 keV photon energy with the above elucidated technique. The magnification plane was perpendicular to the axis of rotation. Figure 5 shows the reconstruction of a sagittal and axial section of the drill. In the sagittal plane the vertical resolution is about 5.6 µm while the horizontal resolution is about 150 nm, respectively. In the axial plane the two-dimensional resolution is about 150 nm. Green coloured tubular pores with dimensions below 1 µm diameter can be seen. In addition the refraction enhanced contrast at the outer edges and around the pores is visible.

4. Conclusions

X-ray refraction techniques combine analytical capabilities of sub-micrometer structure detection with the requirements of non-destructive full volume characterization. Its potential of contrasting cracks and pores will be an alternative to other attempts on raising the spatial resolution of CT machines. Even beyond the spatial resolution of the detector and the reconstruction an average crack densities can be determined. The techniques are expected to close an essential gap in the spectrum of non-destructive techniques for a better understanding of micro structures of materials down to the nanometre scale and their behaviour under thermal and mechanical loads. X-ray refraction therefore might help accelerating materials development, better understanding meso-structures and partly replace micro analysis and mechanical testing in advanced materials science.

Acknowledgements

The authors wish to acknowledge J. Bamberg and F. Heutling from MTU Aero Engines for financial support and for making available the LCP specimens.

References

1. AH Compton and SK Allison, 'X-rays in Theory and Experiment', Macmillan, London, 1935.
2. MP Hentschel, R Hosemann, A Lange, B Uther, R Brückner, ′Röntgenkleinwinkelbrechung an Metalldrähten, Glasfäden und hartelastischem Polypropylen', Acta Crystallographica A, Vol 43, p 506, 1987.
3. K-W Harbich, MP Hentschel, J Schors, 'X-ray refraction characterization of non-metallic materials', NDT&E International, Vol 34, p 297, 2001.
4. A Guinier and G Fournet, 'Small-Angle Scattering of X-Rays', Wiley, New York, 1955.
5. G Porod, ′Röntgenkleinwinkelstreuung von dichtgepackten kolloidalen Systemen, 1. Teil', Kolloid-Zeitschrift, Vol 124, p 83, 1951.
6. W Görner, MP Hentschel, BR Müller, H Riesemeier, M Krumrey, G Ulm, W Diete, U Klein, R Frahm, ′BAMline: the first hard X-ray beamline at BESSY II', Nucl. Inst. Meth. A, Vol 467, pp 703-706, 2001.
7. BR Müller, A Lange, M Harwardt, MP Hentschel, B Illerhaus, J Goebbels, J Bamberg, F Heutling, 'Refraction computed tomography - Application to metal matrix composites', Materialprüfung /Materials Testing, Vol 46, p 314, 2004.
8. D Chapman, W Thomlinson, ER Johnston, D Washburn, E Pisano, N Gmur, Z Zhong, R Menk, F Arfelli, D Sanyers, 'Diffraction enhanced X-ray imaging', Phys. Med Biol, Vol 42, pp 2015 – 2025, 1997.
9. A Koch, C Raven, P Spanne, A Snigirev, 'X-ray imaging with sub micrometer resolution employing transparent luminescent screens', J. Opt. Soc. Am., Vol 15, No 7, pp 1940-1951, 1998.
10. E Förster, K Goetz, P Zaumseil, Kristall und Technik, Vol 15, pp 937 – 945, 1980.
11. R Köhler and P Schäfer, Cryst. Res. Technol., Vol 37, No 7, pp 734 – 746, 2002.